



Ingeniously enhanced ferromagnetism in chemically-reduced 2D $\text{Ti}_3\text{C}_2\text{T}_x$ MXene

Tej B. Limbu^{a,b,**}, Shalini Kumari^{c,d}, Ziqiao Wang^c, Chetan Dhital^e, Qi Li^c, Yongan Tang^f, Fei Yan^{a,*}

^a Department of Chemistry and Biochemistry, North Carolina Central University, Durham, NC, 27707, USA

^b Department of Physical and Applied Sciences, University of Houston-Clear Lake, Houston, TX, 77058, USA

^c Department of Physics, The Pennsylvania State University, University Park, PA, 16802, USA

^d Department of Materials Science & Engineering, The Pennsylvania State University, University Park, PA, 16802, USA

^e Department of Physics, Kennesaw State University, Marietta, GA, 30060, USA

^f Department of Mathematics and Physics, North Carolina Central University, Durham, NC, 27707, USA

HIGHLIGHTS

- Ferromagnetic hysteresis loops were observed for reduced $\text{Ti}_3\text{C}_2\text{T}_x$ up to 150 K.
- L-ascorbic acid treatment is a promising approach for enhancing magnetism in MXenes.
- Chemical reduction enables novel 2D magnetic materials for spintronic applications.

ABSTRACT

Chemical reduction is a facile and cost-effective technique for the modulation of the physical and chemical properties of nanomaterials. Herein, we demonstrate an enhancement of the magnetic behavior of $\text{Ti}_3\text{C}_2\text{T}_x$ MXene after its chemical reduction via L-ascorbic acid treatment. Small ferromagnetic loops have been observed below 50 K for $\text{Ti}_3\text{C}_2\text{T}_x$ prepared by hydrofluoric acid (HF) etching of Al layers from Ti_3AlC_2 . Such a ferromagnetic ordering of spins was significantly enhanced via a chemical reduction of $\text{Ti}_3\text{C}_2\text{T}_x$ with L-ascorbic acid. Ferromagnetic hysteresis loops were observed for reduced $\text{Ti}_3\text{C}_2\text{T}_x$ ($r\text{-Ti}_3\text{C}_2\text{T}_x$) up to 150 K indicating a significant upshift of the paramagnetic to the ferromagnetic transition temperature, pushing towards room temperature. The enhancement of ferromagnetism and upshift of the ferromagnetic transition temperature could be attributed to the localized unpaired electron in Ti-3d orbital of the $r\text{-Ti}_3\text{C}_2\text{T}_x$ crystal and increase in the number of unsaturated Ti atoms upon L-ascorbic acid treatment. Chemical reduction via L-ascorbic acid treatment shows a promising pathway towards the modulation and enhancement of magnetism in various MXene materials for the development of 2D metallic soft ferromagnets and spintronic devices.

1. Introduction

Recent developments in miniaturized, ultra-low power, and low-cost memory and spintronic devices have allowed the field of 2D magnetic materials to advance rapidly [1,2]. Several 2D van der Waals (vdW) materials [3] such as CrI_3 , [4] PtSe_2 [5], VSe_2 [6], MnSe_2 [7], NiPS_3 [8], FePS_3 [9], Fe_3GeTe_2 , [10] $\text{Cr}_2\text{Ge}_2\text{Te}_6$ [11], CrGeTe_3 , and CrSiTe_3 [12], with intrinsic magnetic properties have been fabricated in laboratories and investigated, however, further modifications of the magnetic properties to realize strong magnetization is sorely needed for their practical applications. It has been reported that defect engineering can induce [5,13,14] and modulate [15] the magnetism in 2D vdW

materials. However, creation of the defects in 2D crystals significantly ruins their other intrinsic properties such as electrical and thermal conductivities [16,17], optical properties [18], and mechanical strength [19]. Such an obstacle stimulates exploration of novel materials that have rooms for a state-of-art modification of the crystal chemistry to modulate the magnetic properties without degrading other novel functional properties.

MXenes [20,21], a new intriguing family of highly conductive and super-hydrophilic 2D materials, have been extensively explored for various applications. Recent theoretical predictions [22–25] and experimental studies [26–31] on the magnetism of $\text{Ti}_3\text{C}_2\text{T}_x$ have portrayed MXenes as promising 2D magnetic materials. One of the key

* Corresponding author.

** Corresponding author. Department of Chemistry and Biochemistry, North Carolina Central University, Durham, NC, 27707, USA.

E-mail addresses: limbu@uhcl.edu (T.B. Limbu), fyan@nccu.edu (F. Yan).

<https://doi.org/10.1016/j.matchemphys.2022.126155>

Received 5 July 2021; Received in revised form 7 March 2022; Accepted 16 April 2022

Available online 25 April 2022

0254-0584/© 2022 Elsevier B.V. All rights reserved.

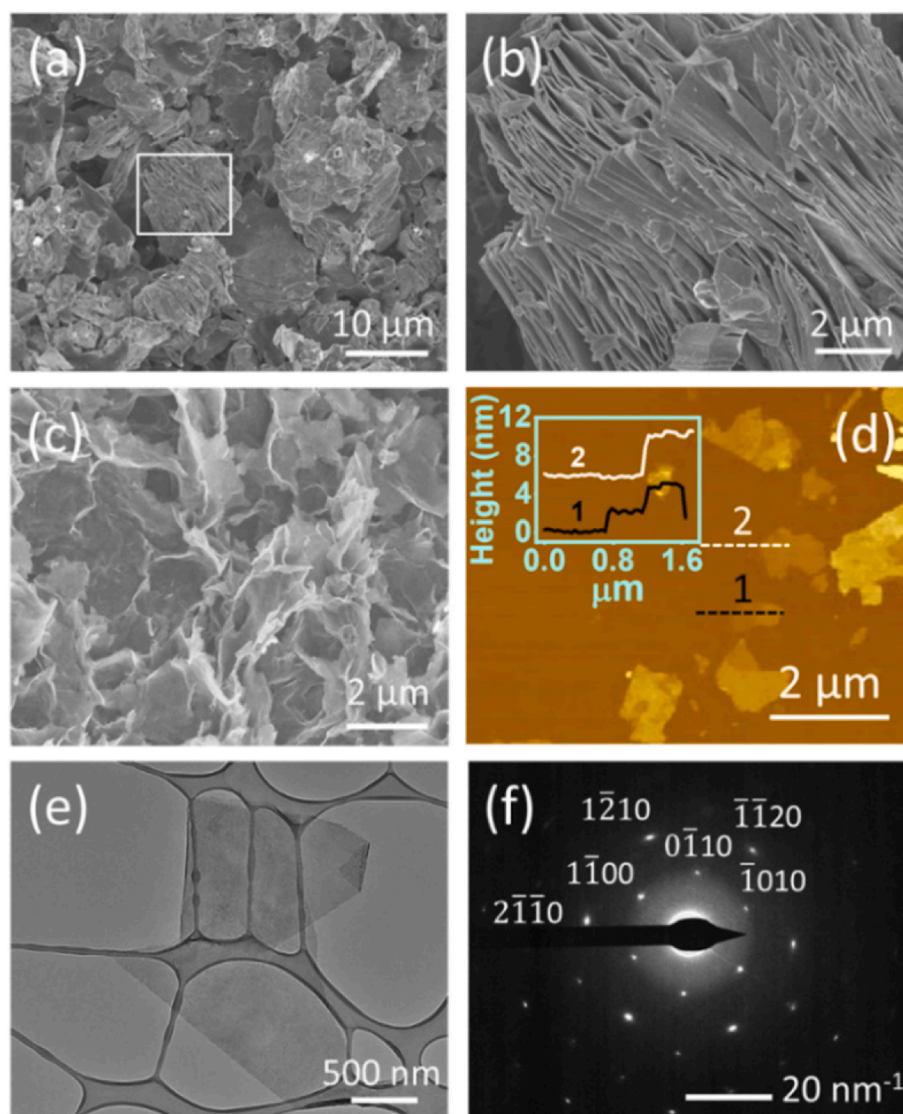


Fig. 1. SEM micrograph of (a) multilayered- $\text{Ti}_3\text{C}_2\text{T}_x$ crystals after HF etching of Ti_3AlC_2 MAX phase, (b) multilayered- $\text{Ti}_3\text{C}_2\text{T}_x$ crystal showing the accordion-like structure, and (c) $\text{Ti}_3\text{C}_2\text{T}_x$ powder. (d) Tapping mode AFM image of $\text{Ti}_3\text{C}_2\text{T}_x$ nanosheets on SiO_2/Si , (e) high magnification TEM image of a $\text{Ti}_3\text{C}_2\text{T}_x$ nanosheet suspended over a holey carbon grid, and (f) selected area electron diffraction (SAED) pattern of the nanosheet shown in Fig. 1e.

differences between MXenes and other 2D vdW materials is that the former's surface is terminated with various functional groups, these include $-\text{F}$, $-\text{OH}$, and $-\text{O}$ [20,21], which are directly bonded to Ti atoms of the crystal. Further studies show that removal or alteration of the surface terminations of MXenes modifies the electronic [21,32] and magnetic [23,29,30] properties. Limbu et al. [21] have demonstrated that reduction of $\text{Ti}_3\text{C}_2\text{T}_x$ via *L*-ascorbic acid treatment modulates the surface structure of the crystal and hence the electronic properties, which are manifested as an enhanced electrical conductivity and oxidation resistance of the material. Combining all these recent findings, modulation of the magnetic properties of $\text{Ti}_3\text{C}_2\text{T}_x$ can also be expected, which would be very desirable for practical applications if the magnetic behavior of the crystal is improved.

Herein, we report the direct observation of weak ferromagnetism in $\text{Ti}_3\text{C}_2\text{T}_x$ prepared by etching Al layers from the Ti_3AlC_2 MAX phase and enhancement of the ferromagnetism after its termination engineering via chemical reduction. The reduction of $\text{Ti}_3\text{C}_2\text{T}_x$ was carried out by treating the MXene with an environmentally friendly and mild reducing agent, *L*-ascorbic acid, which has already been proved to have a good enough reducing capability for nanomaterials synthesis and tailoring their properties [33–35]. The study shows that *L*-ascorbic acid treatment

can be a facile and safe pathway to acquire metallic soft ferromagnets and 2D spintronic materials for practical applications.

2. Experimental

$\text{Ti}_3\text{C}_2\text{T}_x$ and *r*- $\text{Ti}_3\text{C}_2\text{T}_x$ were synthesized following the protocols from our previous paper, with a slight modification [21]. Briefly, 0.5 g of Ti_3AlC_2 (Carbon-Ukraine, Y-Carbon, Ltd) crystals were etched out for 7 h using 10 ml of 30% HF solution (ACROS Organics, 48–51% solution in water) to remove Al layers. The mixture was then washed by vacuum filtration using a stericup with a polyvinylidene difluoride (PVDF) (MilliporeSigma) with deionized (DI) water until its pH reached ~ 6 and dried in a vacuum desiccator. Two conical flasks were cleaned, and in each of the flasks, 100 mg of the dried powder was added to 50 ml of 25 mM tetrabutylammonium hydroxide (TBAOH) (Alfa Aesar, Electronic grade, 99.9999% (metals basis)) liquid solution and stirred in a shaker for 24 h to exfoliate $\text{Ti}_3\text{C}_2\text{T}_x$ nanosheets. Subsequently, the exfoliated $\text{Ti}_3\text{C}_2\text{T}_x$ nanosheets were centrifuged at 3500 rpm for 5 min to separate the unetched MXene particles. The colloidal solution of $\text{Ti}_3\text{C}_2\text{T}_x$ nanosheets was then washed several times by centrifuging at 3500 rpm for 30 min until the pH of the supernatant solution was decreased to ~ 7 .

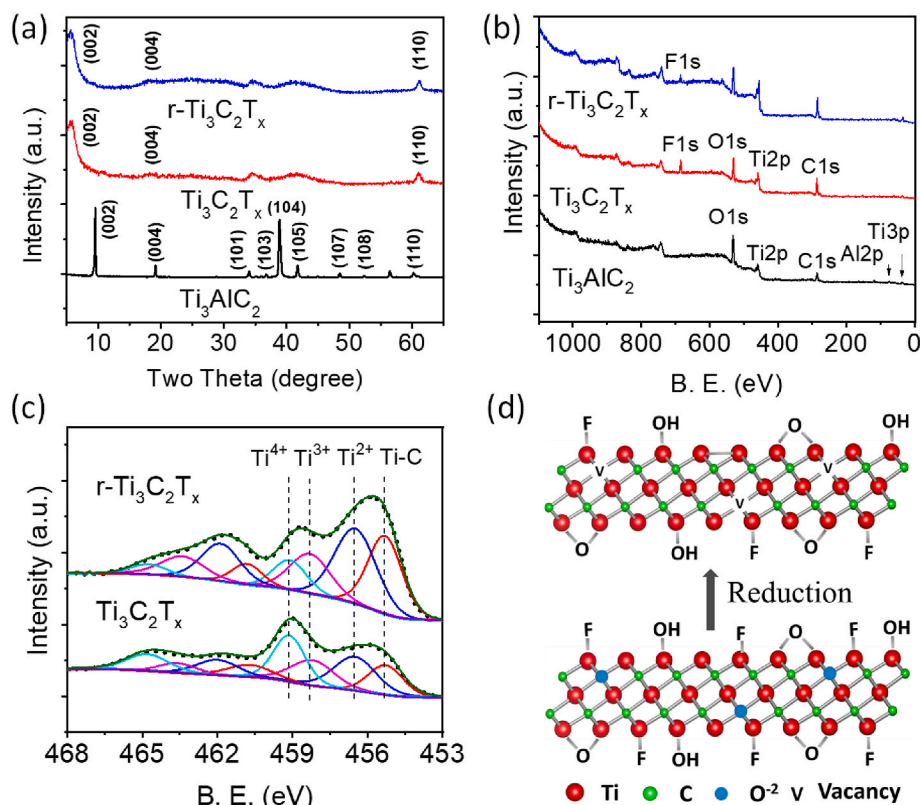


Fig. 2. (a) XRD patterns of Ti_3AlC_2 , $\text{Ti}_3\text{C}_2\text{T}_x$, and $r\text{-Ti}_3\text{C}_2\text{T}_x$, (b) XPS survey spectra of Ti_3AlC_2 , $\text{Ti}_3\text{C}_2\text{T}_x$, and $r\text{-Ti}_3\text{C}_2\text{T}_x$, (c) XPS Ti2p core-level lines of $\text{Ti}_3\text{C}_2\text{T}_x$, and $r\text{-Ti}_3\text{C}_2\text{T}_x$, and (d) schematic diagram for the crystal structure and surface chemistry of $\text{Ti}_3\text{C}_2\text{T}_x$, and $r\text{-Ti}_3\text{C}_2\text{T}_x$.

One batch of the $\text{Ti}_3\text{C}_2\text{T}_x$ was freeze-dried to obtain $\text{Ti}_3\text{C}_2\text{T}_x$ powder and the other was further processed to obtain $r\text{-Ti}_3\text{C}_2\text{T}_x$ powder. For reduction, the black-colored clay of the cleaned $\text{Ti}_3\text{C}_2\text{T}_x$ nanosheets was mixed with 80 ml of water containing 1 g of L-ascorbic acid (Fisher Scientific, Reagent Grade) and stirred for 8 h in a shaker. Finally, L-ascorbic acid was removed by several rounds of centrifugation, and the cleaned slurry was freeze-dried to obtain $r\text{-Ti}_3\text{C}_2\text{T}_x$ powder. Finally, the obtained powders of $\text{Ti}_3\text{C}_2\text{T}_x$ and $r\text{-Ti}_3\text{C}_2\text{T}_x$ nanosheets were stored in a vacuum desiccator to minimize further contamination and surface oxidation.

X-ray diffraction (XRD) (Rigaku SmartLab X-ray Diffractometer) was used for structural analysis. Atomic force microscopy (AFM) (Horiba Smart SPM) was used in tapping mode to measure the height profile of the exfoliated MXene nanosheets. Scanning electron microscopy (SEM) (FEI Verios 460 L operating at 2 kV with 13 pA current) and transmission electron microscopy (TEM) (FEI Talos F200X, 200 KV accelerating voltage) were employed for imaging of the nanosheets. X-ray photoelectron microscopy (XPS) (SPECS FlexMod XPS, Mg Ka excitation (1254 eV)) was employed for elemental analysis and for the confirmation of chemical reduction of $\text{Ti}_3\text{C}_2\text{T}_x$. XPS core-level lines were deconvoluted using Voigt functions with CasaXPS software. To increase the accuracy of the XPS peak deconvolution, individual Voigt functions with similar full width at half maximum (FWHM) have been used. Temperature and magnetic field dependence of *dc* magnetization measurements of MXene powders were performed in a wide temperature range of 5–350 K with a Quantum Design Magnetic Property Measurement System (MPMS).

3. Results and discussion

3.1. Synthesis and characterization of $\text{Ti}_3\text{C}_2\text{T}_x$ and $r\text{-Ti}_3\text{C}_2\text{T}_x$

Fig. 1a shows an SEM micrograph of the multilayered- $\text{Ti}_3\text{C}_2\text{T}_x$

crystals obtained after the HF etching of Ti_3AlC_2 powder. An accordion-like structure is evident on the high magnification SEM micrograph shown in Fig. 1b, which indicates a successful etching of Al layers from the Ti_3AlC_2 crystals [36]. A fabric-like structures observed in the SEM micrograph (Fig. 1c) further indicates that the $\text{Ti}_3\text{C}_2\text{T}_x$ nanosheets were delaminated successfully by TBAOH molecules intercalation [21]. The majority of the $\text{Ti}_3\text{C}_2\text{T}_x$ nanosheets were measured to have a thickness ranging from ~ 1.6 to ~ 4.5 nm corresponding to 2 to 6 layers. Fig. 1e depicts a high magnification TEM image of a $\text{Ti}_3\text{C}_2\text{T}_x$ nanosheet and a representative selected area electron diffraction (SAED) pattern in Fig. 1f shows a six-fold reflection spot corresponding to the hexagonal crystal symmetry of $\text{Ti}_3\text{C}_2\text{T}_x$.

Fig. 2a shows the XRD patterns of Ti_3AlC_2 , $\text{Ti}_3\text{C}_2\text{T}_x$, and $r\text{-Ti}_3\text{C}_2\text{T}_x$. Several peaks of Ti_3AlC_2 including the most intense one at 39.0° are not observed for $\text{Ti}_3\text{C}_2\text{T}_x$, and $r\text{-Ti}_3\text{C}_2\text{T}_x$, due to the disappearance of the non-basal crystal planes upon removal of Al layers by HF etching. We observed significant peak broadening and loss of intensity of the peaks (001) such as (002) and (004), and a huge shift of (002) peak at 9.5° for Ti_3AlC_2 occurs to about 6.5° for $\text{Ti}_3\text{C}_2\text{T}_x$ and $r\text{-Ti}_3\text{C}_2\text{T}_x$, due to the removal of Al layers and introduction of functional terminations, consistent with the reports [21,37,38]. No significant differences in the XRD patterns were observed for $\text{Ti}_3\text{C}_2\text{T}_x$, and $r\text{-Ti}_3\text{C}_2\text{T}_x$ since no change in the crystal structure was expected during the chemical reduction.

XPS has been used as a reliable tool to analyze the chemical composition of the MXenes. For example, the XPS survey spectrum (Fig. 2b) of $\text{Ti}_3\text{C}_2\text{T}_x$ does not show Al2p peak that appears at 73 eV ³⁶ in the spectrum of Ti_3AlC_2 MAX phase, which indicates a successful removal of Al layers from the MAX phase by HF etching. Moreover, the spectrum of $\text{Ti}_3\text{C}_2\text{T}_x$ shows a peak corresponding to Fluorine at 685.0 eV with 8.6 atomic%, due to the addition of F surface termination during HF etching [21,37]. After reduction with L-ascorbic acid, the F peak intensity is reduced to 4.0% in the survey spectrum for $r\text{-Ti}_3\text{C}_2\text{T}_x$, indicating that a significant amount of F terminations are removed.

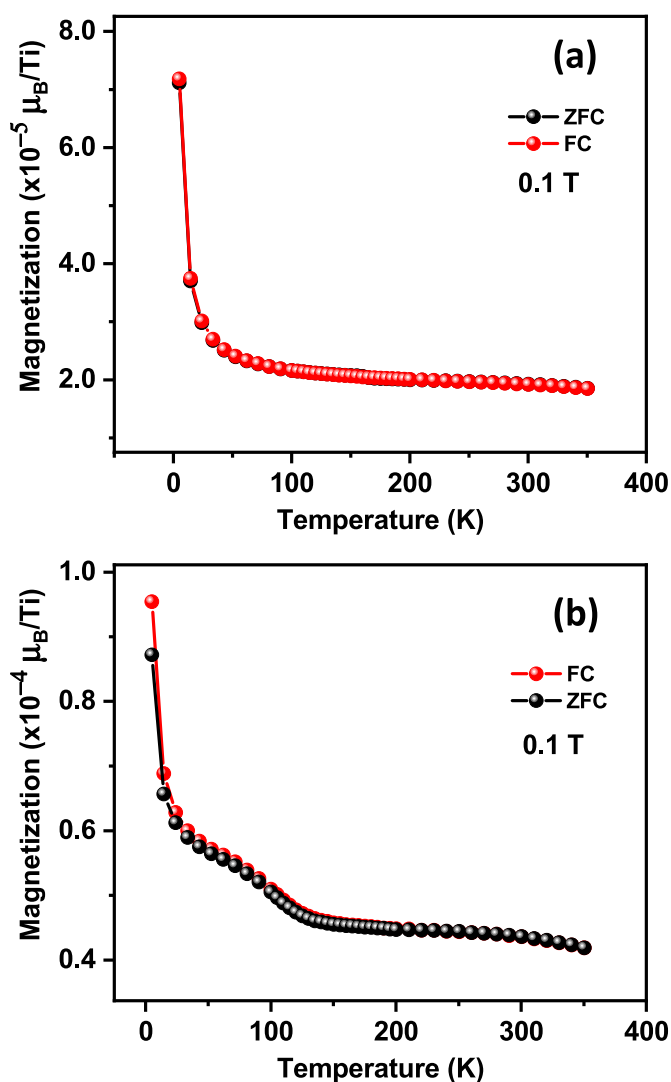


Fig. 3. Temperature dependent magnetization of $\text{Ti}_3\text{C}_2\text{T}_x$ and $r\text{-Ti}_3\text{C}_2\text{T}_x$ in the presence of dc magnetic field of 0.1 T and FC (field-cooled) modes. The corresponding graphs with magnetization expressed in emu/g are shown in Fig. S4, Supporting Information.

XPS Ti2p core-level analysis for $\text{Ti}_3\text{C}_2\text{T}_x$ and $r\text{-Ti}_3\text{C}_2\text{T}_x$ provides more detailed information on the reduction by L-ascorbic acid treatment as shown in Fig. 2c. XPS C1s, O1s, and F1s core-level lines of $\text{Ti}_3\text{C}_2\text{T}_x$ and $r\text{-Ti}_3\text{C}_2\text{T}_x$ and their deconvolutions are presented in Fig. S1, S2, and S3 (Supporting Information), respectively. The atomic% and peak positions of the possible chemical components present in $\text{Ti}_3\text{C}_2\text{T}_x$ and $r\text{-Ti}_3\text{C}_2\text{T}_x$ are presented in Table S1 and S2, respectively. As it is evident that the Ti2p peak for both $\text{Ti}_3\text{C}_2\text{T}_x$ and $r\text{-Ti}_3\text{C}_2\text{T}_x$ has spin-orbit components, Ti2p_{3/2} and Ti2p_{1/2} separated by ~ 5.5 eV. Each doublet component Ti2p_{3/2} (Ti2p_{1/2}) can be deconvoluted into four different chemical components peaking at 455.3 (460.8), 456.6 (462.0), 458.2 (463.5), and 459.2 (464.8) eV, and have been assigned to Ti – C, Ti^{2+} , Ti^{3+} , and Ti^{4+} chemical states, respectively [21,26,39]. The observed peak positions of the individual Ti – C, Ti^{2+} , Ti^{3+} , and Ti^{4+} chemical states of Ti are consistent with those of other compounds, such as TiC [40], Pt/Meso-TiO₂-SiO₂ [41], amorphous sodium titanate [42], and Na₂Ti₃O₇ [43], respectively. The comparison of the two Ti2p core-level lines reveals that the amount of Ti^{4+} chemical state decreases and Ti^{3+} increases in $r\text{-Ti}_3\text{C}_2\text{T}_x$ as compared to that of $\text{Ti}_3\text{C}_2\text{T}_x$. This suggests that a large amount of Ti^{4+} chemical state in $\text{Ti}_3\text{C}_2\text{T}_x$ is mainly contributed by the Ti atoms surrounded by oxygen ions (O^{2-}) in the lattice, which could take

place due to the removal of some carbon atoms and replacement by O^{2-} during the etching process [21,26]. The removal of some carbons from the crystal could also cause the significant broadening of the XRD peak as discussed above. During the reduction by L-ascorbic acid treatment, the O^{2-} are removed [21,26]. A schematic diagram for the crystal structure and surface chemistry of $\text{Ti}_3\text{C}_2\text{T}_x$ and $r\text{-Ti}_3\text{C}_2\text{T}_x$ is presented in Fig. 2d.

3.2. Magnetic properties of $\text{Ti}_3\text{C}_2\text{T}_x$ and $r\text{-Ti}_3\text{C}_2\text{T}_x$

Fig. 3 shows the temperature-dependent magnetization of $\text{Ti}_3\text{C}_2\text{T}_x$ and $r\text{-Ti}_3\text{C}_2\text{T}_x$ samples with the applications of dc magnetic field of ~ 0.1 T (T), under both ZFC (zero-field cooled).

For both $\text{Ti}_3\text{C}_2\text{T}_x$ and $r\text{-Ti}_3\text{C}_2\text{T}_x$ samples, the magnetization gradually decreases with the increase of temperature in both FC and ZFC modes. The M vs. T curves for $\text{Ti}_3\text{C}_2\text{T}_x$ and $r\text{-Ti}_3\text{C}_2\text{T}_x$ in Fig. 3a and b, respectively, show that magnetization on these materials is small with a maximum value, $7.0 \times 10^{-5} \mu_B/\text{Ti}$ for $\text{Ti}_3\text{C}_2\text{T}_x$, and $9.0 \times 10^{-5} \mu_B/\text{Ti}$ for $r\text{-Ti}_3\text{C}_2\text{T}_x$ at 5 K and at 0.1 T. Considering such a small magnetization in our samples, it is apparent that the M-T curves for $\text{Ti}_3\text{C}_2\text{T}_x$ and $r\text{-Ti}_3\text{C}_2\text{T}_x$ (Fig. 3a and b) look slightly different. The curves are smooth and both ZFC-FC branches almost coincide for $\text{Ti}_3\text{C}_2\text{T}_x$, whereas the curves of $r\text{-Ti}_3\text{C}_2\text{T}_x$ show some anomaly and the ZFC-FC branches slightly bifurcate below 140 K. Such an anomaly and a slight bifurcation of the M vs. T curve observed for $r\text{-Ti}_3\text{C}_2\text{T}_x$ could be attributed to the changes in the surface terminations of $r\text{-Ti}_3\text{C}_2\text{T}_x$ with respect to $\text{Ti}_3\text{C}_2\text{T}_x$ and changes in the magnetic behavior of the sample below 140 K. Furthermore, a larger value of magnetization observed for $r\text{-Ti}_3\text{C}_2\text{T}_x$ as compared to that of $\text{Ti}_3\text{C}_2\text{T}_x$ for the same applied field of 0.1 T indicates that the effective number of Bohr magnetons increases in the reduced sample.

Fig. 4a and b shows the magnetic hysteresis (M – H) loops for $\text{Ti}_3\text{C}_2\text{T}_x$ and $r\text{-Ti}_3\text{C}_2\text{T}_x$ measured at different temperatures ranging from 5 to 350 K. The M – H loops with magnetization expressed in emu/g are shown in Fig. S5, Supporting Information. Both $\text{Ti}_3\text{C}_2\text{T}_x$ and $r\text{-Ti}_3\text{C}_2\text{T}_x$ show a weak magnetic response, and the magnetization (M) keeps increasing almost linearly with the applied magnetic field as measured up to 2 T (not shown here), which is indicative of the large paramagnetic response on top of the ferromagnetic signal in $\text{Ti}_3\text{C}_2\text{T}_x$ and $r\text{-Ti}_3\text{C}_2\text{T}_x$ under high magnetic fields. Observation of such hysteresis loops in a wide range of temperatures is consistent with the previous reports [29, 30] on 500 °C H₂-annealed $\text{Ti}_3\text{C}_2\text{T}_x$ and differently functionalized $\text{Ti}_3\text{C}_2\text{T}_x$ samples. Furthermore, the observed loops for both $\text{Ti}_3\text{C}_2\text{T}_x$ and $r\text{-Ti}_3\text{C}_2\text{T}_x$ are not saturated up to the highest magnetic field we have measured, due to the paramagnetic background.

We also note that M – H measurement with an empty capsule (without a magnetic sample) usually produces a small ferromagnetic-like loop, which might originate from the remnant magnetization of the coils in Quantum design MPMS. Such a magnetic contribution could obscure the magnetic behavior of weak magnetic materials like MXenes, and hence it should always be subtracted. Thus, to study the source of the magnetic loop and extract the ferromagnetic-like contribution of MXenes, we subtracted the linear background contributed by the paramagnetic component and the ferromagnetic-like loop obtained in M – H measurement with the empty capsule. After subtraction of the linear background and magnetic loop obtained with empty capsule, purely ferromagnetic hysteresis loops were obtained for both $\text{Ti}_3\text{C}_2\text{T}_x$ and $r\text{-Ti}_3\text{C}_2\text{T}_x$ as shown in Fig. 4c and d, respectively, and the loops for $\text{Ti}_3\text{C}_2\text{T}_x$ above 50 K and those of $r\text{-Ti}_3\text{C}_2\text{T}_x$ above 150 K vanish. More importantly, the hysteresis loops are saturated at a certain value of the applied magnetic field. Hence, it is evident that there is always a ferromagnetic ordering of spins for $\text{Ti}_3\text{C}_2\text{T}_x$ and $r\text{-Ti}_3\text{C}_2\text{T}_x$ at and below 50 K and 150 K, respectively, which vanishes at higher temperatures because of the thermal agitation that tends to misalign magnetic moments in neighboring regions and the long-range order is destroyed [44]. The disappearance of the ferromagnetic loops above 50 and 150 K for $\text{Ti}_3\text{C}_2\text{T}_x$ and $r\text{-Ti}_3\text{C}_2\text{T}_x$, respectively, suggest that paramagnetic to ferromagnetic

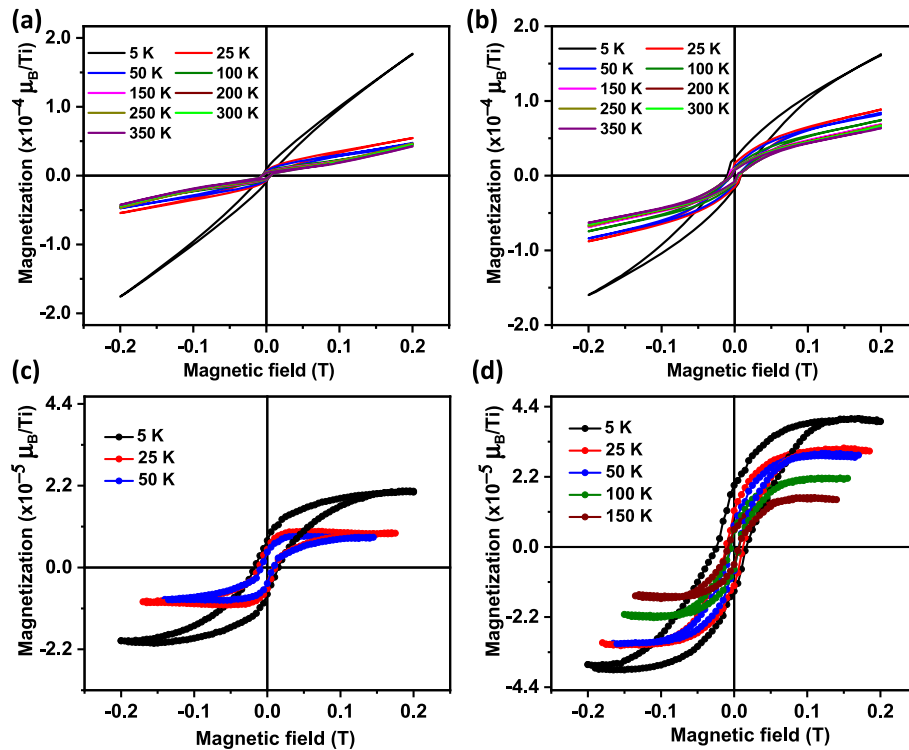


Fig. 4. Magnified curves for the field-dependent magnetization of (a) $\text{Ti}_3\text{C}_2\text{T}_x$ and (b) $r\text{-Ti}_3\text{C}_2\text{T}_x$ at various temperatures. Magnetic hysteresis loops of (c) $\text{Ti}_3\text{C}_2\text{T}_x$ and (d) $r\text{-Ti}_3\text{C}_2\text{T}_x$ obtained after subtraction of linear paramagnetic background and ferromagnetic-like background loop observed with the empty capsule.

transition in $\text{Ti}_3\text{C}_2\text{T}_x$ and $r\text{-Ti}_3\text{C}_2\text{T}_x$ occurs at or around 50 and 150 K, respectively. This conclusion can also be correlated to the M-T curves in Fig. 3a and b, where ZFC and FC branches overlap for $\text{Ti}_3\text{C}_2\text{T}_x$ and slightly bifurcate below 140 K for $r\text{-Ti}_3\text{C}_2\text{T}_x$. Although small ferromagnetic loops are observed for $\text{Ti}_3\text{C}_2\text{T}_x$ at and below 50 K, no bifurcation of the ZFC and FC branches is observed, which may be accounted for the predominant Curie-like paramagnetic behavior of the sample [45].

Fig. 4c and d shows a significantly enhanced ferromagnetic loops for $r\text{-Ti}_3\text{C}_2\text{T}_x$ as compared to that of $\text{Ti}_3\text{C}_2\text{T}_x$. Please see Fig. S6, Supporting Information for M – H loops with magnetization measured in emu/g. We extracted the values of saturation magnetization (M_s), remnant magnetization (M_r), and coercive field (H_c) of both the samples and are presented in Fig. 5. It is evident that M_s and M_r values for $r\text{-Ti}_3\text{C}_2\text{T}_x$ are about 2–3 times larger than that of $\text{Ti}_3\text{C}_2\text{T}_x$, indicating a significant enhancement of the ferromagnetic ordering of the spins upon L-ascorbic acid treatment. On the other hand, the value of H_c for $r\text{-Ti}_3\text{C}_2\text{T}_x$ is slightly larger than that for $\text{Ti}_3\text{C}_2\text{T}_x$ at 5 K, while the value is about the same for higher temperatures.

Overall, M_s and M_r values are enhanced significantly in $r\text{-Ti}_3\text{C}_2\text{T}_x$ maintaining the value of H_c for higher temperatures. Such a conducting material with ferromagnetic behavior with a small H_c is useful for designing spin-valve devices [46]. It is worth noting that the value of M_r , $2.0 \times 10^{-5} \mu_B/\text{Ti}$ (~ 0.002 emu/g) is greater than those of 500 °C H_2 -annealed $\text{Ti}_3\text{C}_2\text{T}_x$ and differently functionalized $\text{Ti}_3\text{C}_2\text{T}_x$ samples, which suggests that the chemical reduction via L-ascorbic acid treatment can be a facile and effective route for enhancing the magnetism in $\text{Ti}_3\text{C}_2\text{T}_x$.

It has been reported that parent material MAX Ti_3AlC_2 is Pauli paramagnetic [47,48] whose magnetic susceptibility is temperature independent. Theoretical investigations [49–52] reveal that non-terminated Ti_3C_2 MXene is ferromagnetic and fully functionalized $\text{Ti}_3\text{C}_2\text{T}_x$ is nonmagnetic. However, $\text{Ti}_3\text{C}_2\text{T}_x$ prepared by using various etching methods, chemicals, and doping have been reported to exhibit different magnetic nature. For example, Iqbal et al. [27] found a weak ferromagnetic ordering in an undoped $\text{Ti}_3\text{C}_2\text{T}_x$ and observed an

exchange bias effect due to the co-existence of FM-AFM phases in lanthanum-doped $\text{Ti}_3\text{C}_2\text{T}_x$. Zhang et al. [29] observed evolution of ferromagnetism in $\text{Ti}_3\text{C}_2\text{T}_x$ upon H_2 annealing at 500 °C, due to the introduction of Ti and C vacancy pairs in some specific configurations. On the other hand, Scheibe et al. [30] reported an antiferromagnetic-paramagnetic (AFM-PM) states in the $\text{Ti}_3\text{C}_2\text{T}_x$ prepared by using both HF and chlorosulfonic acid, and Allen-Perry et al. [31] also suggested a paramagnetic-antiferromagnetic (PM-AFM) phase transition in (LiF + HCl)-etched $\text{Ti}_3\text{C}_2\text{T}_x$, and the transition temperature was dependent on Al etching time.

Herein, we present a qualitative explanation for our observation of weak ferromagnetism below 50 K in $\text{Ti}_3\text{C}_2\text{T}_x$, and its enhancement upon L-ascorbic acid treatment, based on our XPS data, changes in the crystal chemistry taking place during solution processing of MXene and its reduction, and previously published results. We follow a model explained in the report [26] for $\text{Ti}_3\text{C}_2\text{T}_x$ crystal chemistry and subsequent changes upon reduction process. According to the report [26], some carbons are removed from $\text{Ti}_3\text{C}_2\text{T}_x$ crystals during Al etching and those vacant sites are occupied by O^{2-} ions. Hence, in our work, the observation of Ti^{4+} valence state in XPS Ti2p core-level line (see Fig. 2c) can be accounted for the regions in the crystal where two of the Ti – C chemical bonds are broken during Al layer etching by HF and the two carbon sites are taken by two O^{2-} ions as $\text{O}^{2-} - \text{Ti}^{4+} - \text{O}^{2-}$ [26]. The regions in the crystal where one Ti – C bond is broken and the carbon site is taken by an O^{2-} ion, Ti ion carries an oxidation state of +2 as $\text{Ti}^{2+} - \text{O}^{2-}$ as observed in Fig. 2c. Some regions where surface Ti atoms are bonded to hydroxide or fluorine (surface termination), lose one of the carbons and the vacant site is taken by an O^{2-} ion, the resulting Ti ion carries an oxidation state of +3 as $\text{O}^{2-} - \text{Ti}^{3+} - \text{OH}^-$ or $\text{F}^- - \text{Ti}^{3+} - \text{O}^{2-}$ (see Fig. 2c). While we consider substitution of carbons site by O^{2-} ions, there may also be some carbon vacant sites remaining unoccupied, which leave the surrounding Ti atoms unsaturated. Such unsaturated Ti atoms with unpaired electrons in their d orbitals have single occupancy of localized states near the Fermi level, which may be correlated to the presence of small initial magnetic moments in $\text{Ti}_3\text{C}_2\text{T}_x$ [29]. This

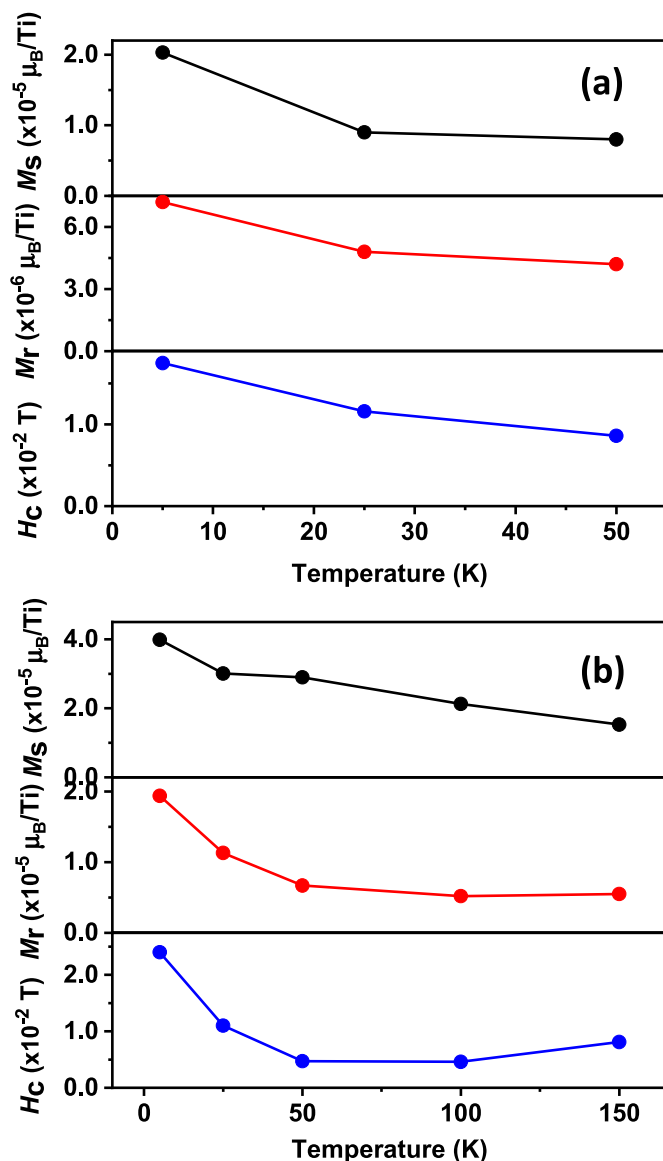


Fig. 5. The saturation magnetization (M_s), remnant magnetization (M_r), and coercive field (H_c) of (a) $\text{Ti}_3\text{C}_2\text{T}_x$, and (b) $r\text{-Ti}_3\text{C}_2\text{T}_x$ at various temperatures.

reasoning can be meaningful if we critically look back at the previous reports [28,30], where surface-terminated $\text{Ti}_3\text{C}_2\text{T}_x$ was observed to have shown paramagnetic and even small ferromagnetic moments but were left unexplained. However, with our model, the origin of the initial magnetic moment in surface terminated $\text{Ti}_3\text{C}_2\text{T}_x$ can be realized. The assignment of unsaturated Ti atoms surrounding the carbon vacancies to the origin of magnetic moment in $\text{Ti}_3\text{C}_2\text{T}_x$ is also in line with the previous computational reports [49–51], where a pristine Ti_3C_2 with unsaturated surface Ti atoms exhibited intrinsic ferromagnetism, with a magnetic moment of $\sim 0.74 \mu_B$ per Ti atom, and the moment disappeared when the surface Ti atoms were saturated with functional terminations such as O, OH, and F. The presence of weak ferromagnetism below 50 K in our $\text{Ti}_3\text{C}_2\text{T}_x$ sample might be due to partial ordering of the spin moments associated with the unpaired electron in unsaturated Ti atoms.

When the $\text{Ti}_3\text{C}_2\text{T}_x$ nanosheets are reduced with L-ascorbic acid, two main changes occur: (1) although 100% is usually unlikely for a bulk of nanosheets, the O^{2-} ions occupying the carbon vacancy sites in the $\text{Ti}_3\text{C}_2\text{T}_x$ crystal are removed [26] from $\text{Ti}_3\text{C}_2\text{T}_x$ nanosheets and a higher oxidation state of Ti is reduced to a lower oxidation state, which is

manifested as a decrease in Ti^{4+} peak and significant increase in the Ti^{3+} peak in the XPS Ti2p core-level line of $r\text{-Ti}_3\text{C}_2\text{T}_x$, and (2) about 50% of the F-terminations are removed. Such a removal of O^{2-} ions and F-terminations cause the increase in the population of unsaturated Ti atoms in the $r\text{-Ti}_3\text{C}_2\text{T}_x$ crystal. The unbonded situation of the Ti atoms could also facilitate the formation of Ti–Ti metallic bonds in $r\text{-Ti}_3\text{C}_2\text{T}_x$ crystals. In other words, due to the missing hybridized Ti3d–C2p and Ti3d–F2p states, either unbonded Ti atoms are left with a localized electron [29] or redistribution of Ti3d–Ti3d metallic bond states near the Fermi energy occurs, thereby increasing the DOS at the Fermi level [21]. As reported previously [21], the increased electron DOS at the Fermi level due to the formation of Ti3d–Ti3d metallic bond states enhances the electrical conductivity in the $r\text{-Ti}_3\text{C}_2\text{T}_x$. On the other hand, the number of unbonded/unsaturated Ti atoms surrounding a carbon vacancy and possessing an unpaired electron/s in Ti3d orbital is increased in $r\text{-Ti}_3\text{C}_2\text{T}_x$ as compared to $\text{Ti}_3\text{C}_2\text{T}_x$, which could explain the increased magnetic moment in $r\text{-Ti}_3\text{C}_2\text{T}_x$. To emphasize our argument, we would like to restate the outcome of previous computational works on pristine $\text{Ti}_3\text{C}_2\text{T}_x$ [49–51], which revealed that the ferromagnetic ordering of the spin moments occurs on the unsaturated Ti atoms within each external Ti sheet whereas interlayer interaction occurring between the opposite Ti sheets is antiferromagnetic, and the combination results in a net ferromagnetic moment on the crystal. From this statement, it can be inferred that the increased number of unsaturated Ti surrounding carbon vacancies is responsible for the enhancement of ferromagnetic moment in $r\text{-Ti}_3\text{C}_2\text{T}_x$. Future experiments correlating the concentration of unsaturated Ti in $r\text{-Ti}_3\text{C}_2\text{T}_x$ to the size of the ferromagnetic moment are necessary for the definite conclusion of this scenario.

The enhancement of the overall magnetic moment in $r\text{-Ti}_3\text{C}_2\text{T}_x$ as compared to $\text{Ti}_3\text{C}_2\text{T}_x$ is well-correlated to our XPS results. Literature reports [50,53–56] show that Ti^{3+} and Ti^{2+} valence states of Ti are responsible for a magnetic moment and ferromagnetic polarization in their compounds/materials, and Ti^{4+} valence state contributes to no moment. Our XPS results revealed that the ratio of the Ti^{2+} valence state to Ti–C state in $\text{Ti}_3\text{C}_2\text{T}_x$ (~ 1.3) remains virtually the same after ascorbic acid treatment (~ 1.4). We note that Ti–C in the XPS core-level line of Ti2p represents the Ti valence state in which Ti atom is surrounded only by C atoms, which should remain intact after ascorbic acid treatment because no additional C or Ti atoms are expected to chemically combine with Ti or C atoms in the crystal. As evident in Fig. 2c, the amount of Ti^{2+} valence state is identical to that of Ti–C in both $\text{Ti}_3\text{C}_2\text{T}_x$ and $r\text{-Ti}_3\text{C}_2\text{T}_x$, indicating that further reduction of Ti^{3+} to Ti^{2+} valence state does not happen. This may be because Ti^{2+} is a powerful reducing agent which could not be produced by a mild reducing agent such as ascorbic acid. So what changes is only the relative amount of Ti^{4+} and Ti^{3+} valence states. As evident in Fig. 2c, the amount of Ti^{4+} decreases and the amount of Ti^{3+} increases during the reduction by ascorbic acid, which may contribute to the enhancement of the magnetism in $r\text{-Ti}_3\text{C}_2\text{T}_x$.

A final note is, although measured moments in $\text{Ti}_3\text{C}_2\text{T}_x$ and $r\text{-Ti}_3\text{C}_2\text{T}_x$ (in emu/g) (see Figs. S4, S5, and S6, Supporting Information) are comparable to the values reported previously [27,29–31], our measured ferromagnetic moments expressed as $(0.8 - 2.1) \times 10^{-5} \mu_B/\text{Ti}$ atom for $\text{Ti}_3\text{C}_2\text{T}_x$ and $(1.5 - 4.0) \times 10^{-5} \mu_B/\text{Ti}$ atom for $r\text{-Ti}_3\text{C}_2\text{T}_x$ look much smaller than the calculated value $\sim 0.74 \mu_B/\text{Ti}$ atom [49,51] for pristine Ti_3C_2 system. The calculated value of moments presented in previous computational studies represents the value expected in each unsaturated Ti in a pristine and free-standing graphene-like Ti_3C_2 system, i.e., without any functional groups. The values obtained from the bulk magnetization measurements in the present work represent the net moment present in non-freestanding MXene in the partial presence of functional groups, i.e., neighboring two or more MXene nanocrystals might be interacting. We should also note that the net magnetization in a material system depends upon the orientation of magnetic moments present in the magnetic atoms or ions. For example, in a system with

large canted magnetic moments, it is not uncommon to see small net ferromagnetic magnetization [57–59]. However, it is difficult to mention exact magnetic structure of $\text{Ti}_3\text{C}_2\text{T}_x$ and $r\text{-Ti}_3\text{C}_2\text{T}_x$ and orientation of the moments at this point based on our observations. An analysis with magnetic neutron or magnetic x-ray scattering is desirable to correlate the net bulk moment to the individual moments from unsaturated Ti atoms in MXene systems and can be suggested for future studies.

4. Conclusion

Predominantly few-layered $\text{Ti}_3\text{C}_2\text{T}_x$ nanosheets were prepared by HF etching of Al layers from Ti_3AlC_2 MAX phase, and the nanosheets were reduced chemically by using L-ascorbic acid as a reducing agent. Magnetic properties of the dried powders of both $\text{Ti}_3\text{C}_2\text{T}_x$ and $r\text{-Ti}_3\text{C}_2\text{T}_x$ were studied in detail using MPMS. The results showed that as-prepared $\text{Ti}_3\text{C}_2\text{T}_x$ possesses weak ferromagnetic ordering of spins at low temperatures below 50 K. However, $r\text{-Ti}_3\text{C}_2\text{T}_x$ showed significantly enhanced ferromagnetism that survives up to 150 K, which could be attributed to the localized unpaired electron on Ti3d orbital of the $r\text{-Ti}_3\text{C}_2\text{T}_x$ crystal and increase in the number of unsaturated Ti atoms upon L-ascorbic acid treatment. Our findings provide useful insights for modulating the magnetic behavior in MXenes by a chemical reduction for the development of novel 2D magnetic materials for spintronic applications such as spin-valve devices.

CRedit authorship contribution statement

Tej B. Limbu: Conceptualization, Methodology, Writing – original draft, Writing – review & editing. **Shalini Kumari:** Methodology, Investigation, Writing – review & editing. **Ziqiao Wang:** Investigation. **Chetan Dhital:** Validation. **Qi Li:** Resources, Writing – review & editing. **Yongan Tang:** Resources. **Fei Yan:** Supervision, Writing – review & editing, Funding acquisition.

Declaration of competing interest

The authors declare that they have no known competing financial interests or personal relationships that could have appeared to influence the work reported in this paper.

Acknowledgments

The authors, T. B. L., Y. T., and F. Y. are grateful for the financial support of this project by the U.S. National Science Foundation (Awards # 1831133, #1523617, #2122044). Q. L., Z. W., and S. K. would like to thank DOE FG02-08ER46531 and NSF Award #1905833. MPMS facility is supported by NSF MRSEC under the grant numbers, DMR-1420620 and DMR-1523617. This work was performed in part at the Analytical Instrumentation Facility (AIF) at North Carolina State University, which is supported by the State of North Carolina and the National Science Foundation (award number ECCS-1542015). The AIF is a member of the North Carolina Research Triangle Nanotechnology Network (RTNN), a site in the National Nanotechnology Coordinated Infrastructure (NNCI).

Appendix A. Supplementary data

Supplementary data related to this article can be found at <https://doi.org/10.1016/j.matchemphys.2022.126155>.

References

- [1] K.S. Burch, D. Mandrus, J.G. Park, Magnetism in two-dimensional van der Waals materials, *Nature* 563 (2018) 47–52.
- [2] N. Samarth, Condensed-matter physics, Magnetism in flatland *Nature* 546 (2017) 216–218.

- [3] M.C. Wang, C. Huang, C.H. Cheung, C.Y. Chen, S.G. Tan, T.W. Huang, Y. Zhao, G. Wu, Y.P. Feng, H.C. Wu, Prospects and opportunities of 2D van der Waals magnetic systems, *Ann. Phys.* 532 (2020) 1900452.
- [4] C. Gong, et al., Discovery of intrinsic ferromagnetism in two-dimensional van der Waals crystals, *Nature* 546 (2017) 265–269.
- [5] A. Avsar, A. Ciarracchi, M. Pizzochero, D. Unuchek, O.V. Yazyev, A. Kis, Defect induced, layer-modulated magnetism in ultrathin metallic PtSe_2 , *Nat. Nanotechnol.* 14 (2019) 674–678.
- [6] M. Bonilla, et al., Strong room-temperature ferromagnetism in VSe_2 monolayers on van der Waals substrates, *Nat. Nanotechnol.* 13 (2018) 289–293.
- [7] D.J. O'Hara, et al., Room temperature intrinsic ferromagnetism in epitaxial manganese selenide films in the monolayer limit, *Nano Lett.* 18 (2018) 3125–3313.
- [8] C.T. Kuo, et al., Exfoliation and Raman spectroscopic fingerprint of few-layer NiPS_3 van der Waals crystals, *Sci. Rep.* 6 (2016) 20904.
- [9] J.-U. Lee, et al., Ising-type magnetic ordering in atomically thin FeP_3 , *Nano Lett.* 16 (2016) 7433–7438.
- [10] Z. Fei, et al., Two-dimensional itinerant ferromagnetism in atomically thin Fe_3GeTe_2 , *Nat. Mater.* 17 (2018) 778–782.
- [11] B. Huang, et al., Layer-dependent ferromagnetism in a van der Waals crystal down to the monolayer limit, *Nature* 546 (2017) 270–273.
- [12] M.W. Lin, et al., Ultrathin nanosheets of CrSiTe_3 : a semiconducting two-dimensional ferromagnetic material, *J. Mater. Chem. C* 4 (2016) 315–322.
- [13] O.V. Yazyev, L. Helm, Defect-induced magnetism in graphene, *Phys. Rev. B* 75 (2007) 125408.
- [14] Z. Guguchia, A. Kerelsky, D. Edelberg, S. Banerjee, F. von Rohr, D. Scullion, M. Augustin, M. Scully, D.A. Rhodes, Z. Shermadini, H. Luetkens, Magnetism in semiconducting molybdenum dichalcogenides, *Sci. Adv.* 4 (2018) 3672.
- [15] M. Pizzochero, Atomic-scale defects in the two-dimensional ferromagnet CrI_3 from first principles, *J. Phys. Appl. Phys.* 53 (2020) 244003.
- [16] Y.V. Skrypnik, V.M. Loktev, Electrical conductivity in graphene with point defects, *Phys. Rev. B* 82 (2010), 085436.
- [17] T.B. Limbu, K.R. Hahn, F. Mendoza, S. Sahoo, J. Razink, R.S. Katiyar, B.R. Weiner, G. Morell, Grain size-dependent thermal conductivity of polycrystalline twisted bilayer graphene, *Carbon* 117 (2017) 367–375.
- [18] W. Wang, H. Shu, J. Wang, Y. Cheng, P. Liang, X. Chen, Defect passivation and photoluminescence enhancement of monolayer MoS_2 crystals through sodium halide-assisted chemical vapor deposition growth, *ACS Appl. Mater. Interfaces* 12 (2020) 9563–9571.
- [19] A. Zandiataashbar, G.H. Lee, S.J. An, S. Lee, N. Mathew, M. Terrones, T. Hayashi, C. R. Picu, J. Hone, N. Koratkar, Effect of defects on the intrinsic strength and stiffness of graphene, *Nat. Commun.* 5 (2014) 1–9.
- [20] M. Khazaei, A. Mishra, N.S. Venkataramanan, A.K. Singh, S. Yunoki, Recent advances in MXenes: from fundamentals to applications, *Curr. Opin. Solid State Mater. Sci.* 23 (2019) 164–178.
- [21] T.B. Limbu, B. Chitara, J.D. Orlando, M.Y.G. Cervantes, S. Kumari, Q. Li, Y. Tang, F. Yan, Green synthesis of reduced $\text{Ti}_3\text{C}_2\text{T}_x$ MXene nanosheets with enhanced conductivity, oxidation stability, and SERS activity, *J. Mater. Chem. C* 8 (2020) 4722–4731.
- [22] M. Khazaei, A. Ranjbar, M. Arai, T. Sasaki, S. Yunoki, Electronic properties and applications of MXenes: a theoretical review, *J. Mater. Chem. C* 5 (2017), 2488–250.
- [23] N.C. Frey, A. Bandyopadhyay, H. Kumar, B. Anasori, Y. Gogotsi, V.B. Shenoy, Surface-engineered MXenes: electric field control of magnetism and enhanced magnetic anisotropy, *ACS Nano* 13 (2019) 2831–2839.
- [24] S. Zhao, W. Kang, J. Xue, Manipulation of electronic and magnetic properties of M_2C ($\text{M} = \text{Hf}, \text{Nb}, \text{Sc}, \text{Ta}, \text{Ti}, \text{V}, \text{Zr}$) monolayer by applying mechanical strains, *Appl. Phys. Lett.* 104 (2014) 133106.
- [25] M. Sternik, U.D. Wdowik, Probing the impact of magnetic interactions on the lattice dynamics of two-dimensional Ti_2X ($\text{X} = \text{C}, \text{N}$) MXenes, *Phys. Chem. Chem. Phys.* 20 (2018) 7754–7763.
- [26] Y. Yoon, T.A. Le, A.P. Tiwari, I. Kim, M.W. Barsoum, H. Lee, Low temperature solution synthesis of reduced two dimensional Ti_3C_2 MXene with paramagnetic behaviour, *Nanoscale* 10 (2018) 22429–22438.
- [27] M. Iqbal, J. Fatheema, Q. Noor, M. Rani, M. Mumtaz, R.K. Zheng, S.A. Khan, S. Rizwan, Co-existence of magnetic phases in two-dimensional MXene, *Mater. Today Chem.* 16 (2020) 100271.
- [28] S. Rafiq, S. Awan, R.K. Zheng, Z. Wen, M. Rani, D. Akinwande, S. Rizwan, Novel room-temperature ferromagnetism in Gd-doped 2-dimensional $\text{Ti}_3\text{C}_2\text{T}_x$ MXene semiconductor for spintronics, *J. Magn. Magn. Mater.* 497 (2020) 165954.
- [29] K. Zhang, M. Di, L. Fu, Y. Deng, Y. Du, N. Tang, Enhancing the magnetism of 2D carbide MXene $\text{Ti}_3\text{C}_2\text{T}_x$ by H_2 annealing, *Carbon* 157 (2020) 90–96.
- [30] B. Scheibe, K. Tadzyszak, M. Jarek, N. Michalak, M. Kempinski, M. Lewandowski, B. Peplińska, K. Chybczyńska, Study on the magnetic properties of differently functionalized multilayered $\text{Ti}_3\text{C}_2\text{T}_x$ MXenes and Ti-Al-C carbides, *Appl. Surf. Sci.* 479 (2019) 216–224.
- [31] K. Allen-Perry, W. Straka, D. Keith, S. Han, L. Reynolds, B. Gautam, D.E. Autrey, Tuning the magnetic properties of two-dimensional MXenes by chemical etching, *Materials* 14 (2021) 694.
- [32] J.L. Hart, K. Hantanasirisakul, A.C. Lang, B. Anasori, D. Pinto, Y. Pivak, J.T. van Omme, S.J. May, Y. Gogotsi, M.L. Taheri, Control of MXenes' electronic properties through termination and intercalation, *Nat. Commun.* 10 (2019) 1–10.
- [33] M.W. Shah, Y. Zhu, X. Fan, J. Zhao, Y. Li, S. Asim, C. Wang, Facile synthesis of defective TiO_{2-x} nanocrystals with high surface area and tailoring bandgap for visible-light photocatalysis, *Sci. Rep.* 5 (2015) 1–8.
- [34] T.B. Magdaline, A.V. Murugan, Microwave-assisted hydrometallurgical extraction of $\text{Li}_4\text{Ti}_5\text{O}_{12}$ and LiFePO_4 from ilmenite: effect of PPy-Br_2 derived C-coating with N,

- Br, and Nb₅₊ Co-doping on electrodes for high-rate energy storage performance, *Dalton Trans.* 49 (2020) 6227–6241.
- [35] J. Zhang, H. Yang, G. Shen, P. Cheng, J. Zhang, S. Guo, Reduction of graphene oxide via L-ascorbic acid, *Chem. Commun.* 46 (2010) 1112–1114.
- [36] T.B. Limbu, B. Chitara, M.Y. Garcia Cervantes, Y. Zhou, S. Huang, Y. Tang, F. Yan, Unravelling the thickness dependence and mechanism of surface-enhanced Raman scattering on Ti₃C₂T_x MXene nanosheets, *J. Phys. Chem. C* 124 (2020) 17772–17782.
- [37] M. Naguib, M. Kurtoglu, V. Presser, J. Lu, J. Niu, M. Heon, L. Hultman, Y. Gogotsi, M.W. Barsoum, Two-dimensional nanocrystals produced by exfoliation of Ti₃AlC₂, *Adv. Mater.* 23 (2011) 4248–4253.
- [38] X. Zhao, A. Vashisth, E. Prehn, W. Sun, S.A. Shah, T. Habib, Y. Chen, Z. Tan, J. L. Lutkenhaus, M. Radovic, M.J. Green, Antioxidants unlock shelf-stable Ti₃C₂T_x (MXene) nanosheet dispersions, *Matter* 1 (2019) 513–526.
- [39] J. Halim, K.M. Cook, M. Naguib, P. Eklund, Y. Gogotsi, J. Rosen, M.W. Barsoum, X-ray photoelectron spectroscopy of select multi-layered transition metal carbides (MXenes), *Appl. Surf. Sci.* 362 (2016) 406–417.
- [40] L. Zhang, R.V. Koka, A study on the oxidation and carbon diffusion of TiC in alumina–titanium carbide ceramics using XPS and Raman spectroscopy, *Mater. Chem. Phys.* 57 (1998) 23–32.
- [41] Q. Wu, C. Zhang, B. Zhang, X. Li, Z. Ying, T. Liu, W. Lin, Y. Yu, H. Cheng, F. Zhao, Highly-selective Pt/ordered mesoporous TiO₂–SiO₂ catalysts for hydrogenation of cinnamaldehyde: the promoting role of Ti²⁺, *J. Colloid Interface Sci.* 463 (2016) 75–82.
- [42] H. Yang, J.G. Duh, Aqueous sol–gel synthesized anatase TiO₂ nanoplates with high-rate capabilities for lithium-ion and sodium-ion batteries, *RSC Adv.* 6 (2016) 37160–37166.
- [43] A. Rudola, K. Saravanan, C.W. Mason, P. Balaya, Na₂Ti₃O₇: an intercalation based anode for sodium-ion battery applications, *J. Mater. Chem.* 1 (2013) 2653–2662.
- [44] M. Gibertini, M. Koperski, A.F. Morpurgo, K.S. Novoselov, Magnetic 2D materials and heterostructures, *Nat. Nanotechnol.* 14 (2019) 408–419.
- [45] L. Sangaletti, M.C. Mozzati, P. Galinetto, C.B. Azzoni, A. Speghini, M. Bettinelli, G. Calestani, Ferromagnetism on a paramagnetic host background: the case of rutile TM: TiO₂ single crystals (TM= Cr, Mn, Fe, Co, Ni, Cu), *J. Phys. Condens. Matter* 18 (2006) 7643.
- [46] D.H. Han, J.G. Zhu, J.H. Judy, NiFe/NiO bilayers with high exchange coupling and low coercive fields, *J. Appl. Phys.* 81 (1997) 4996–4998.
- [47] P. Finkel, M.W. Barsoum, J.D. Hettinger, S.E. Lofland, H.I. Yoo, Low-temperature transport properties of nanolaminates Ti₃AlC₂ and Ti₄AlN₃, *Phys. Rev. B* 67 (2003) 235108.
- [48] P. Finkel, J.D. Hettinger, S.E. Lofland, M.W. Barsoum, T. El-Raghy, Magnetotransport properties of the ternary carbide (formula presented): hall effect, magnetoresistance, and magnetic susceptibility, *Phys. Rev. B* 65 (2001), 035113.
- [49] I.R. Shein, A.L. Ivanovskii, Graphene-like titanium carbides and nitrides Ti_{n+1}C_n, Ti_{n+1}N_n (n= 1, 2, and 3) from de-intercalated MAX phases: first-principles probing of their structural, electronic properties and relative stability, *Comput. Mater. Sci.* 65 (2012) 104–114.
- [50] F. Wu, K. Luo, C. Huang, W. Wu, P. Meng, Y. Liu, E. Kan, Theoretical understanding of magnetic and electronic structures of Ti₃C₂ monolayer and its derivatives, *Solid State Commun.* 222 (2015) 9–13.
- [51] I.R. Shein, A.L. Ivanovskii, Graphene-like nanocarbitides and nanonitrides of d metals (MXenes): synthesis, properties and simulation, *Micro & Nano Lett.* 8 (2013) 59–62.
- [52] Y. Xie, P.R.C. Kent, Hybrid density functional study of structural and electronic properties of functionalized Ti_{n+1}X_n (X = C, N) monolayers, *Phys. Rev. B* 87 (2013) 235441.
- [53] J.S. Lee, Y.W. Xie, H.K. Sato, C. Bell, Y. Hikita, H.Y. Hwang, C.C. Kao, Titanium d_{xy} ferromagnetism at the LaAlO₃/SrTiO₃ interface, *Nat. Mater.* 12 (2013) 703–706.
- [54] R. Pentcheva, W.E. Pickett, Charge localization or itinerancy at LaAlO₃/SrTiO₃ interfaces: hole polarons, oxygen vacancies, and mobile electrons, *Phys. Rev. B* 74 (2006), 035112.
- [55] J. Xu, D.H. Ji, Z.Z. Li, W.H. Qi, G.D. Tang, X.Y. Zhang, Z.F. Shang, L.L. Lang, Estimate of the cation distribution for Ti-doped Ni_{0.68}Fe_{2.32}O₄ spinel ferrites by fitting magnetic moments at 10 K, *Phys. Status Solidi* 252 (2015) 411–420.
- [56] Y.N. Du, J. Xu, Z.Z. Li, G.D. Tang, J.J. Qian, M.Y. Chen, W.H. Qi, Valence of Ti cations and its effect on magnetic properties of spinel ferrites Ti_xM_{1-x}Fe₂O₄ (M= Co, Mn), *RSC Adv.* 8 (2018) 302–310.
- [57] C. Dhital, S. Khadka, Z. Yamani, C. De La Cruz, T.C. Hogan, S.M. Disseler, M. Pokharel, K.C. Lukas, W. Tian, C.P. Opeil, Z. Wang, Spin ordering and electronic texture in the bilayer iridate Sr₃Ir₂O₇, *Phys. Rev. B* 86 (2012) 100401.
- [58] K. Lu, D. Sapkota, L. DeBeer-Schmitt, Y. Wu, H.B. Cao, N. Mannella, D. Mandrus, A. A. Aczel, G.J. MacDougall, Canted antiferromagnetic order in the monoaxial chiral magnets V_{1/3}TaS₂ and V_{1/3}NbS₂, *Physical Review Materials* 4 (2020), 054416.
- [59] M. Nakano, Y. Wang, S. Yoshida, H. Matsuoka, Y. Majima, K. Ikeda, Y. Hirata, Y. Takeda, H. Wadati, Y. Kohama, Y. Ohigashi, Intrinsic 2D ferromagnetism in V₅Se₈ epitaxial thin films, *Nano Lett.* 19 (2019) 8806–8810.